Local and Equatorial Forcing of Seasonal Variations of the North Equatorial Countercurrent in the Atlantic Ocean

JIAYAN YANG AND TERRENCE M. JOYCE

Department of Physical Oceanography, Woods Hole Oceanographic Institution, Woods Hole, Massachusetts

ABSTRACT

The seasonal variation of the North Equatorial Countercurrent (NECC) in the tropical Atlantic Ocean is investigated by using a linear, one-layer reduced-gravity ocean model and by analyzing sea surface height (SSH) data from Ocean Topography Experiment (TOPEX)/Poseidon (T/P) altimeters. The T/P data indicate that the seasonal variability of the NECC geostrophic transport, between 3° and 10°N, is dominated by SSH changes in the southern flank of the current. Since the southern boundary of the NECC is located partially within the equatorial waveguide, the SSH variation there can be influenced considerably by the equatorial dynamics. Therefore, it is hypothesized that the wind stress forcing along the equator is the leading driver for the seasonal cycle of the NECC transport. The wind stress curl in the NECC region is an important but smaller contributor. This hypothesis is tested by several sensitivity experiments that are designed to separate the two forcing mechanisms. In the first sensitivity run, a wind stress field that has a zero curl is used to force the ocean model. The result shows that the NECC geostrophic transport retains most of its seasonal variability. The same happens in another experiment in which the seasonal wind stress is applied only within a narrow band along the equator outside the NECC range. To further demonstrate the role of equatorial waves, another experiment was run in which the wind stress in the Southern Hemisphere is altered so that the model excludes hemispherically symmetrical waves (Kelvin waves and odd-numbered meridional modes of equatorial Rossby waves) and instead excites only the antisymmetrical equatorial Rossby modes. The circulation in the northern tropical ocean, including the NECC, is affected considerably even though the local wind stress there remains unchanged. All these appear to support the hypothesis presented in this paper.

1. Introduction

The North Equatorial Countercurrent (NECC) is a major component of the upper-ocean circulation in the tropical Atlantic Ocean. It varies profoundly in its seasonal cycle, and even its direction reverses briefly in the spring. Previous studies have shown that the NECC is a wind-driven, geostrophic current, and its seasonal variability is closely tied to the seasonal movement of the intertropical convergence zone (ITCZ). The mean surface velocity field in the tropical Atlantic Ocean computed from ship drift data shows that the NECC is located roughly between 3° and 10°N and is directed eastward against the prevailing trade wind (Richardson and McKee 1984; Richardson and Walsh 1986; Richardson and Reverdin 1987). Two neighboring currents, the

North Equatorial Current (NEC) to its north and the South Equatorial Current (SEC) to its south, are both flowing westward opposite to the NECC. The NECC is robust in the summer and autumn when the ITCZ is located farther north and weak (or even absent) in the winter and spring when the ITCZ is closer to the equator. Although the NECC is forced by wind stress, it plays an important role in the thermohaline circulation (THC) in the Atlantic Ocean (Fratantoni et al. 2000). It connects the North Brazil Current (NBC), a key component of the upper THC limb, to the interior tropical North Atlantic Ocean.

The seasonal circulation in the tropical Atlantic Ocean was studied extensively in 1980s around the period for the Seasonal Response of the Equatorial Atlantic (SEQUAL) program and the Program Francais Ocean et Climat dans l'Atlantique Equatorial (FOCAL). Many of those studies involved analyzing data (Richardson and Walsh 1986; Richardson and McKee 1984; Richardson et al. 1992; Arnault 1987; Katz and Garzoli 1982, 1984), running numerical models

Corresponding author address: Dr. Jiayan Yang, Department of Physical Oceanography, Woods Hole Oceanographic Institution, Woods Hole, MA 02543.
E-mail: jyang@whoi.edu

(Busalacchi and Picaut 1983; Philander and Pacanowski 1986), and comparing model results with data (Richardson and Philander 1987). Although most of these papers examined the variability over the whole tropical Atlantic Ocean, several of them focused specifically on the seasonal NECC variations and thus are most relevant to this study. Garzoli and Katz (1983) analyzed the observed temperature profiles and wind stress to examine the thermocline response to the wind stress variability. They diagnosed the balances in a linear and one-layer vorticity equation derived by Busalacchi and Picaut (1983) in the region between 3° and 9°N. Their analysis indicated that both local wind stress and Rossby waves from the eastern basin contributed to the seasonal variability of the thermocline depth. They showed that the linear balances held reasonably well in the central basin but broke down near the two boundaries. Verdy and Jochum (2005) conducted some OGCM experiments to show that the western areas where the Sverdrup balance breaks down are more extensive in their model than what was diagnosed by Garzoli and Katz (1983) and pointed out that nonlinear dynamics is important there. The western region has been shown to be active in eddy generation induced by barotropic instability (Jochum and Malanotte-Rizzoli 2003). It should be noted that the Sverdrup balance in the central region, shown by Verdy and Jochum (2005), indicates only the forcing of the meridional velocity by the wind stress curl. The variability of the NECC zonal transport does not have to be forced solely by local wind stress even if the Sverdrup relation holds there. From the equatorial wave solution (see Moore and Philander 1977), the ratio between meridional velocity v and zonal velocity u for a long Rossby waves is proportional to the frequency or wavenumber. For a low-frequency wave at the annual period, this ratio is very small. For Kelvin wave, v is zero. So low-frequency equatorial Kelvin and Rossby waves make only a small contribution to the meridional velocity, and the Sverdrup balance can still be valid for determining v even though u is affected by equatorial waves.

It was assumed in previous studies that the seasonal variation of the NECC is forced by wind stress within the NECC latitude band, either due to the local curl or to Rossby waves forced in the eastern basin (Katz 1987; Garzoli and Richardson 1989). The most specific demonstration of this local forcing mechanism was made by Katz (1987) who computed the geostrophic transport of NECC between 3° and 9°N, using data from inverted echo sounder deployment from February 1983 to September 1984, at both 38° and 28°W. He then applied the wind stress forcing in the NECC region to the linear vorticity equation used by Busalacchi and Picaut (1983)

and Garzoli and Katz (1983). The model reproduced well both the phases and the amplitudes of the geostrophic transport derived from the data at both 38° and 28°W. It showed that the NECC transport was forced primarily by the local wind stress curl outside the equatorial region. This conclusion, which has been widely accepted (e.g., see a review paper by Lee and Csanady 1999), will be examined in this study. A recent analysis of satellite sea surface height (SSH) data by Schouten et al. (2005) showed that the seasonal variability of the zonal geostrophic velocity averaged between 4° and 10°N propagates westward from the eastern boundary. They further suggested that the neglect of Rossby waves generated at the eastern boundary in some previous studies, such as the one by Garzoli and Katz (1983), may have contributed to the breakdown of the linear balances in the region to the east of 30°W. Schouten et al.'s study implies a role of the equatorial forcing since Rossby waves radiated from the eastern boundary often resulted from reflection of equatorial Kelvin waves. Still, how important the remote forcing is as relative to the local forcing has not been quantified.

Rossby waves can be radiated from the eastern boundary either directly forced by alongshore wind or from the reflection of equatorial Kelvin waves. Within the equatorial waveguide, Kelvin and Rossby waves are generated, propagated, and reflected at eastern and western boundaries (Cane and Sarachik 1983). Through the wave propagation, wind stress in the equatorial regions can remotely force variability in regions far away. The NECC is a geostrophic current, so its zonal transport is proportional to the meridional difference of the SSH. Satellite altimetry data indicate that the seasonal variation of this SSH difference is dominated by changes in the southern side of NECC (Fig. 1 for the seasonal variations and Fig. 2 for the standard deviation). Since the NECC is located partially within the equatorial waveguide, defined to the latitudinal band that traps the equatorial Kelvin waves and the gravest modes of equatorial Rossby waves, its variability is inevitably affected by equatorial waves. The equatorial contribution to the NECC seasonal transport has not been explicitly examined and quantified.

The state of knowledge in the NECC research can be summarized as the following: 1) the NECC is a wind-driven geostrophic current, 2) modeling and data analysis studies indicated that the seasonal variability of the NECC transport is forced by both local wind stress curl and remote Rossby waves from the eastern basin, 3) the Sverdrup balance appears to be valid in the central regions and less so near two boundaries, and 4) the nonlinearity becomes important near the western boundary
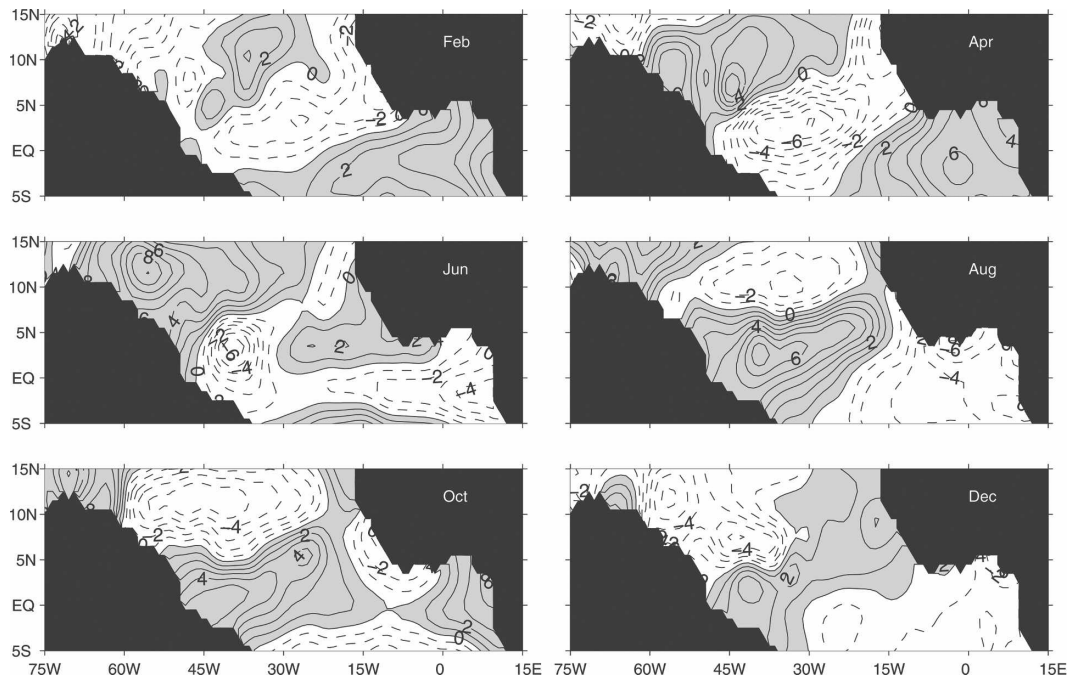
FIG. 1. The SSH climatology derived from the T/P altimeters (contour interval: 2 cm). The dataset is from the gridded 1° × 1° monthly data from NASA Ocean Pathfinder Program. The annual mean is removed.

bacause of the barotropic instability. The equatorial forcing has not been identified as a major forcing mechanism, perhaps because of the strong influence by Katz (1987) who well reproduced the observed NECC transport by invoking the wind stress forcing locally within the NECC latitudinal band. The remote Rossby waves in Katz's model were not originated from the equatorial forcing since the SSH was set to be constant along the eastern boundary and thus disconnected to the equatorial waveguide. A very recent study by
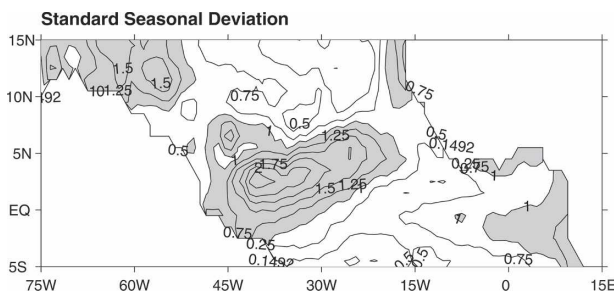

FIG. 2. The standard seasonal deviation of the SSH computed by using observations from the T/P altimeters (areas where SSH deviation is greater than 1 cm are shaded, and the contour interval is 0.25 cm). Note that the high seasonal deviation occurs to the south of NECC and to the north of the equator. The variation to the north of NECC, between 7° and 10°N is much weaker. This suggests that the seasonal variation of the NECC transport is more influenced by changes of SSH in the southern region where the equatorial dynamics plays a leading role.

Schouten et al. (2005) implies a role of equatorial waves since Rossby waves shown in their analysis can be traced to the eastern boundary where the SSH variability could be related to equatorial Kelvin waves. Nevertheless, the role of the equatorial forcing on the seasonal variability of the NECC transport has not been explicitly examined and its importance relative to the local forcing has not been quantified. In this paper we will demonstrate that the remote forcing from the equatorial regions is actually the leading mechanism for the seasonal NECC variability. Our contribution to the NECC research is the explicit examination and quantification of the contributions from the equatorial forcing to the seasonal variability of the NECC transport. The result from this study appears to be at odds with the many previous studies, especially the one by Katz (1987). We will explain the difference in the discussion section.

This study involves analyzing SSH data from Ocean Topography Experiment (TOPEX)/Poseidon (T/P) altimeters and running a simple process model. As for the paper organization, the model and data will be introduced in the next section. Results from the model standard run and three additional sensitivity runs will be shown and compared with the T/P data in section 3. Each of the sensitivity runs is designed to separate the equatorial forcing from the wind stress curl forcing along the NECC. Further discussions and a brief summary will be given in section 4.

2. Model and data

a. Data

Gridded $1° \times 1°$ SSH data from TOPEX/Poseidon altimeters (Koblinsky et al. 1998; data were obtained online at http://iliad.gsfc.nasa.gov) are used in this study. We then calculated a monthly climatology by averaging a 10-yr record from January 1993 to December 2002. The seasonal deviation of SSH from 5°S to 15°N has a typical amplitude of about 6–8 cm (Fig. 1). To examine where the seasonal variability of SSH dominates we computed the standard deviation of the seasonal SSH variability. Figure 2 shows that largest seasonal variability occurs between 0° and 5°N, with the standard deviation as high as 2.25 cm between 45° and 30°W. The seasonal variation is considerably weaker elsewhere. The altimeter data indicate that the seasonal variability of the geostrophic transport, which is proportional to the SSH difference across the NECC, is dominated by the SSH change in the southern side of NECC.

The wind stress data are a combined product of using Special Sensor Microwave Imager (SSM/I) measurement of wind speed and the European Centre for Medium-Range Weather Forecasts (ECMWF) wind direction (Atlas et al. 1993). Previous studies have shown that ocean GCM results forced by this combined wind product compare better with observations than those from the same model being forced by wind products from reanalyses such as ECMWF or the National Centers for Environmental Prediction (NCEP; Liu et al. 1996). A monthly climatology of the wind stress is computed by averaging the monthly data from January 1993 to December 2002, covering the same period for the T/P altimetry data used in this study. The annual mean and seasonal deviations of both wind stress and its curl are shown in Fig. 3. The ITCZ moves to the northernmost position in the summer between July and September and its southernmost position between February and April (Waliser and Gautier 1993). The zonal component of trades along the equator is strong during the northward shift of the ITCZ and weak when the ITCZ is close to the equator.

b. Model

The NECC seasonal cycle described by Richardson and Walsh (1986) from using ship drift data represents the surface velocity field that includes both Ekman and geostrophic velocity components. Although the total transport is believed to be dominated by the geostrophic current, the surface velocity field is affected considerably by the Ekman velocity. Arnault (1987) and Richardson et al. (1992) showed that the spring
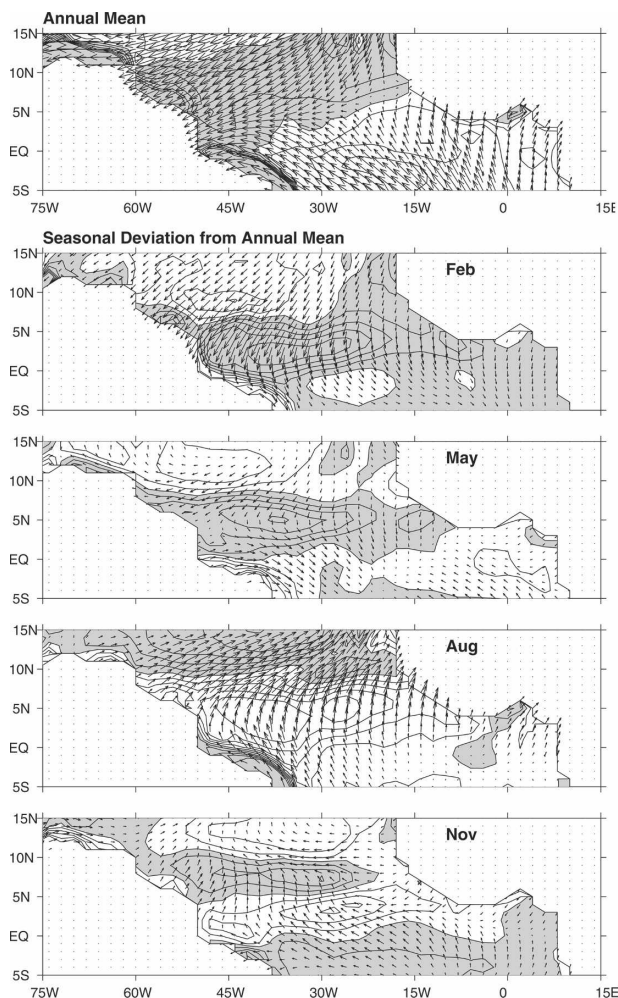

FIG. 3. The surface wind stress and its curl. The wind stress data are a combined product from satellite observation (SSM/I for the wind speed) and ECMWF reanalyses (for the wind direction; Atlas et al. 1993). (The areas of positive curl are shaded; the contour interval is 2×10^{-8} N m^{-3}.)

reversal of NECC in the surface layer was mainly due to the change of the Ekman current. The geostrophic current was much weakened in the spring but nevertheless continued to be eastward. So it is desirable to use a simple model with some representations of both Ekman and geostrophic velocities. For that purpose, we chose the ocean dynamics component of the tropical atmosphere–ocean coupled model developed by Zebiak and Cane (1987). It is a linear reduced-gravity model embedded with a constant-depth (50 m) mixed layer to resolve the depth-averaged Ekman velocity. It assumes that the abyssal layer has an infinite thickness. In this model, an upper layer above the thermocline (thickness of H) is divided into two sublayers, a constant-depth mixed layer with a thickness of $H_m = 50$ m and a subsurface layer (thickness of D, i.e., $H = H_m +$

D). The variations of thermocline depth and the depth-averaged velocity in the whole upper layer (including both sublayers) are computed prognostically by the following equations

$$\frac{\partial u}{\partial t} - fv + g'\frac{\partial h}{\partial x} = A_H \nabla^2 u + \frac{\tau^x}{\rho H}, \tag{1}$$

$$\frac{\partial v}{\partial t} + fu + g'\frac{\partial h}{\partial y} = A_H \nabla^2 v + \frac{\tau^y}{\rho H}, \quad \text{and} \tag{2}$$

$$\frac{\partial h}{\partial t} + H\left(\frac{\partial u}{\partial x} + \frac{\partial v}{\partial y}\right) = 0, \tag{3}$$

where h is the layer thickness anomaly. The following parameter values, $H = 150$ m, $H_m = 50$ m, and $D = H - H_m = 100$ m, are chosen based on the vertical distribution of the geostrophic velocity in the NECC region (Garzoli and Katz 1983). The velocity $\mathbf{u}$ solved from (1) to (2) is the averaged velocity between two sublayers:

$$\mathbf{u} = (H_m \mathbf{u}_m + D\mathbf{u}_D)/H, \tag{4}$$

where $\mathbf{u}_D$ is the velocity in the lower sublayer and is driven by the pressure gradient, and $\mathbf{u}_m$ is the mixed layer velocity that includes both the Ekman $\mathbf{u}_e$ and pressure gradient–driven $\mathbf{u}_D$ velocity components. The Ekman velocity component is solved diagnostically by the following equations:

$$\gamma_e u_e - fv_e = \tau^x/(\rho H) \quad \text{and} \tag{5}$$

$$\gamma_e v_e + fu_e = \tau^y/(\rho H). \tag{6}$$

In (1)–(6) we use the following parameter values: $\gamma_e = 1/(2$ days), the same as what was used in the original Zebiak–Cane model, and $A_H = 10^3$ m^2 s^{-1} for the lateral viscosity. The reduced gravity g' is chosen so that the shallow-water gravity wave speed $c = (g'H)^{1/2} = 1.3$ m s^{-1}. This corresponds to the second baroclinic mode. The decay scale in the equatorial ocean is $L_{eq} = (c/\beta)^{1/2}$, which is about 240 km for $c = 1.3$ m s^{-1} (Moore and Philander 1977). For the first-meridional-mode Rossby waves, the maximum pressure centers are located roughly about $1.5L_{eq}$, about 360 km away from the equator. This is roughly the southern position of NECC. For higher-meridional-mode Rossby waves, the pressure centers are located farther away from the equator.

McCreary et al. (1984) used a three-dimensional dynamical model with the observed density field and found that sea level variability in the tropical Atlantic Ocean is dominated by the second baroclinic mode. The contribution from the first and third modes is only one-third of sea level variation. Based on this finding,

Busalacchi and Picaut (1983) chose parameters in their one-layer reduced-gravity model to simulate only the second-mode responses to observed wind stress in the tropical Atlantic Ocean. The model results compared well with the seasonal cycle of the dynamic height derived from the observed data. The choices of our model parameter values are based on these previous studies. We decide to use linear dynamics for the purpose of using the simplest possible model to address the leading dynamical processes. The use of a linear model can be justified by the success and experiences of previous studies. Busalacchi and Picaut (1983) used the same linear model and simulated a seasonal cycle of the dynamical height in the tropical Atlantic Ocean that compared well with observations. Garzoli and Katz (1983) found that the linear balances in the vorticity equation, as diagnosed from hydrographic data, hold well in the NECC region away from two boundaries. Near the western boundary, the nonlinearity becomes more important as demonstrated in an OGCM simulation by Verdy and Jochum (2005). A realistic coastline is used for the lateral boundary along which no-normal-flow and no-slip boundary conditions are applied. The model is coded in spherical coordinates and has a spatial resolution of 0.5° and a temporal resolution of 30 min. The model extends from 25°S to the 25°N and an open-boundary condition is applied along both latitudes.

3. Model results

The model results will be presented in this section. We will discuss first the output from the "standard run" in which the full wind stress with the annual mean is included (Fig. 3). Three additional sensitivity runs will be introduced and in each of them the forcing field will be altered to elucidate the roles of local and equatorial forcing mechanisms. The monthly wind stress data that were gridded on a 1° × 1° resolution are linearly interpolated into each model time–space grid.

a. Standard run

In the first run, the model (1)–(6) is forced by the wind stress (the annual mean included) shown in Fig. 3. This experiment will be referred to as the standard run to distinguish itself from the sensitivity experiments. The mixed layer velocity, $\mathbf{u}_m$, which includes both Ekman and non-Ekman components, is shown in Fig. 4 for February, May, August, and November. These months and the domain of the plot from 20°S to 20°N were chosen so that one can compare directly with the observed velocity field derived from ship drift data by
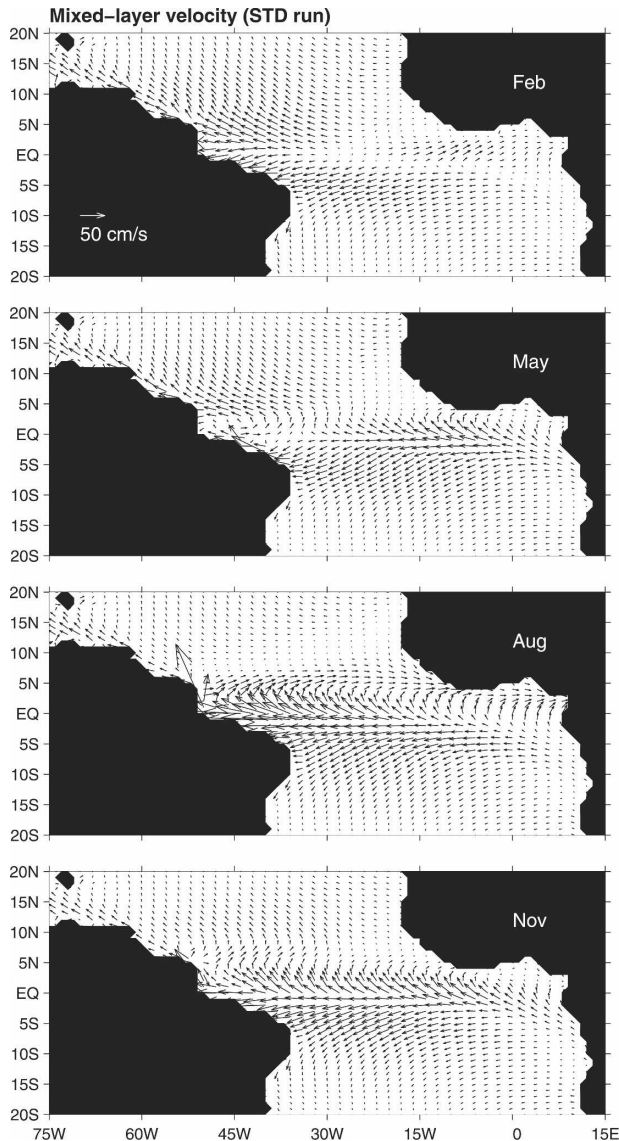
Mixed–layer velocity (STD run)

FIG. 4. The oceanic current in the surface mixed layer (both Ekman and geostrophic components) in February, May, August, and November. The seasonal variation of the NECC is similar to the velocity field derived from ship drift data except that the westward flow along the equator and the western boundary current are too weak in the model. This is likely due to the absence of the model representation of THC, which is a main component of the cross-equatorial flow in the Atlantic Ocean. The annual mean is included in this plot.

Richardson and Walsh (1986). The simple linear model simulates reasonably well the seasonal cycle of surface circulation. For instance, the NECC strengthens in the summer season (all seasons are boreal), extending across the basin and even flowing into the Gulf of Guinea in August. This feature compares well with that from Richardson and Walsh (1986). In winter the NECC weakens substantially and even reverses its di-

rection. This seasonal reversal, considered as a key feature of the NECC seasonal cycle, is simulated by this simple model. Over the whole model domain, however, there are some noticeable differences between model and ship drift data. The western boundary current in the Northern Hemisphere is considerably weaker in the model simulation, and this is likely due to the absence of THC. In the real ocean, there is a strong northward flow along the western boundary in the upper layer that represents the upper limb of the THC. The THC is not forced by the local wind stress, so it is not represented in the model. Including the THC in a model would result in a much stronger northward western boundary current in the tropical Atlantic Ocean (Fratantoni et al. 2000). Another major discrepancy occurs to the zonal current along the equator. It reverses its direction to eastward in February in the model simulation while ship drift data indicate that it should be westward all year. This may also be related to the absence of the THC in the model. The westward zonal current along the equator is fed by the equatorward flow of the SEC from the Southern Hemisphere. The SEC consists of both wind-driven and THC components, so one would expect that the SEC and the westward current along the equator would be weaker in a model that is forced only by the wind stress. It is encouraging, however, to see that most of these discrepancies occur outside of the NECC band.

The seasonal variation of $\mathbf{u}_m$ is most profound in the NECC and in equatorial zonal currents. It is rather small in the area to the north of the NECC. The mixed layer velocity consists of Ekman and non-Ekman components. The Ekman velocity shows a divergence along the equator in all seasons (Fig. 5) and this is certainly due to the westward trade wind along the equator. The seasonal variation of the Ekman velocity is smaller than the total velocity shown in Fig. 4 (note that the scale of velocity vector is different between Figs. 5 and 4). Although the seasonal change of the Ekman velocity is weaker, it is generally in phase with the seasonal cycle of the NECC. For instance, the westward Ekman velocity in the western basin is considerably stronger in the winter and spring months, and thus contributes to the weakening and even reversing of the NECC in those seasons. In the summer, the Ekman velocity is eastward in the central and northeastern tropical region between 0° and 10°N. It even flows into the Gulf of Guinea. This contributes to the seasonally strengthening of NECC in those months. To examine the seasonal changes, we plot the seasonal deviation of the averaged velocity of the whole upper layer [$\mathbf{u} = (H_m\mathbf{u}_m + D\mathbf{u}_D)/H$] from its annual mean. It was shown that the NECC

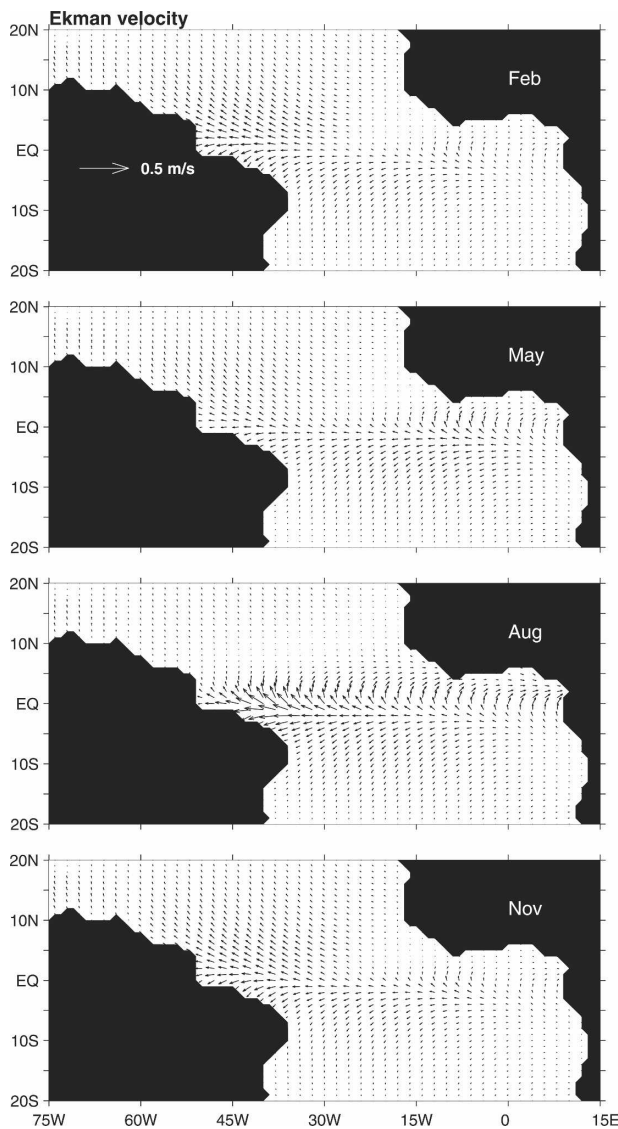FIG. 5. The Ekman component of the mixed layer velocity (annual mean included).

FIG. 6. The seasonal variation of the NECC transport (Sv) between 3° and 10° (solid: total; dash–dotted: Ekman transport; dashed: non-Ekman transport; and dotted: geostrophic transport). Note that the geostrophic transport is much larger than the Ekman transport.

and the zonal current along the equator have the largest seasonal variations.

We have computed the zonal transports of various components between 3° and 10°N at 40°W (Fig. 6a), 30°W (Fig. 6b), and 20°W (Fig. 6c). The total transport (solid lines) that is eastward reaches 15 Sv [1 Sverdrup (Sv) = 1.0×10^6 m^3 s^{-1}] at 40°W in August and September, and 12 Sv at 30°W in August. In April and May the transport becomes westward in those two longitudes, consistent with the observed seasonal reversal of the NECC in the spring. The seasonal variation is small at 20°W where is very close to the eastern boundary. At all three longitudes, the total transport is dominated by the non-Ekman component (i.e., $H\mathbf{u}_D$, dashed lines).
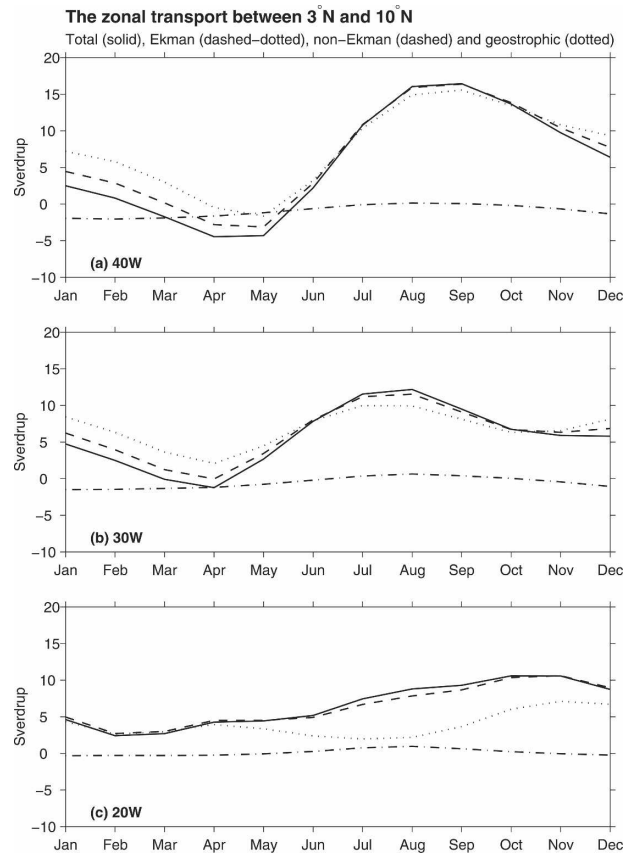
We have also computed the geostrophic transport (dotted lines) by using the model pressure gradient data. At interior locations (40° and 30°W) the geostrophic transport accounts for nearly all of the non-Ekman transport. Very close to the eastern boundary at 20°W, however, the non-Ekman transport is influenced strongly by ageostrophic processes. In all three longitudes, the zonal Ekman transport $H_m u_e$ (dash–dotted lines) is small relative to the total transport (solid lines), consistent with the previous estimate made by Carton and Katz (1990).

Since the geostrophic velocity dominates the seasonal variability of NECC, we will concentrate on its variability in the following discussions. This is also convenient since one can directly compare geostrophic transport estimated from the T/P SSH data. To do so we present here the basinwide distribution of the seasonal SSH variations from the model (Fig. 7). This simple model is doing a reasonable job in simulating large-scale features seen in the T/P data (Fig. 1). Over-
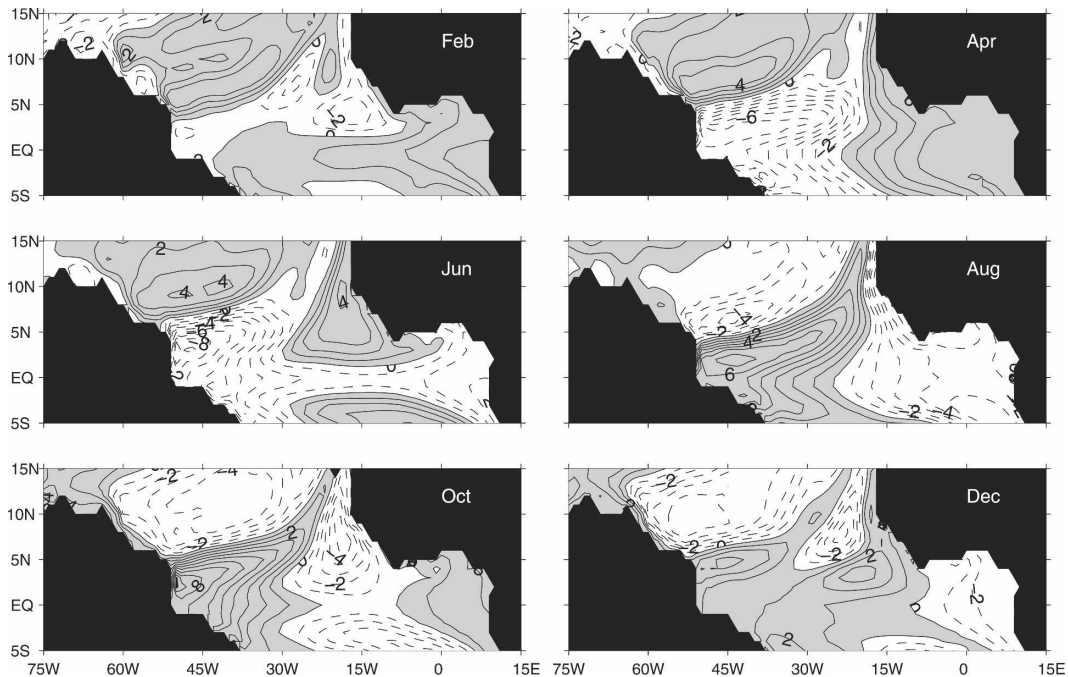
FIG. 7. The seasonal variation of the model SSH (cm). The broad feature is very similar to that from T/P altimetry data (Fig. 1).

all, the model field is much smoother than data. The standard deviation of seasonal SSH variability from the model, shown in Fig. 8a, is similar to that from the altimetry data (Fig. 2). Nevertheless, noticeable differences are obvious. For example, the maximum deviation in the data is located offshore at about 40°W and 2°–3°N, but is right off the western boundary in the model. The discrepancy is probably due to the fact that the tropical Atlantic Ocean has a very broad shelf off the western boundary. Near the equator, for instance, the seafloor is shallower than 200 m in depth within 5°–6° in longitude from the western boundary. The seasonal SSH variability associated with deep-water waves could be attenuated in those shelf regions. In the reduced-gravity model, however, those shallow areas are treated as a deep ocean with an infinite lower-layer thickness. This is the main limitation for using the one-layer reduced-gravity model. While we did not vigorously assess the impact of this model weakness, we speculate that its effect on the NECC in the deep basin is limited based on the success of using a similar model in some previous studies (e.g., Busalacchi and Picaut 1983).

To compare the model geostrophic transport with the T/P SSH data, here we follow Joyce et al. (2004) by defining two boxes, one between 45° and 20°W and between 7° and 10°N and the other between 45° and 20°W and between 1° and 3°N. These two boxes are located on two sides of NECC and the SSH difference is proportional to its geostrophic transport. The main purpose here is to compare the model with data for the bulk properties of the NECC variations averaged over large areas before analyzing individual profiles of zonal velocity across the current and SSH variations at some selected longitudes. Figure 8b shows the seasonal cycle of this SSH difference for both T/P data (thick line) and the model result (thin line). The model agrees quite well with the T/P data in both the amplitude and the phase of time evolution. This gives us a bit more comfort that despite the model weakness and some considerable model–data discrepancies in areas along the equator and the western boundary, the NECC is reasonably well simulated. Figure 8c demonstrates that SSH change from the southern box contributes considerably more to the geostrophic transport than that from the northern box.

To examine the longitudinal variation of the geostrophic transport, we plot the time evolution of the SSH difference (i.e., $\Delta\eta$) between 10° and 3°N across the basin. The annual mean is removed in both model output and in data so that we can focus on the seasonal deviation. The geostrophic transport between these two latitudes is negatively proportional to $\Delta\eta$. The seasonal variation of $\Delta\eta$ is maximum around 40°W and its amplitude is about 10 cm in the T/P data (Fig. 9a). The NECC is weakest (or the least eastward) in May and
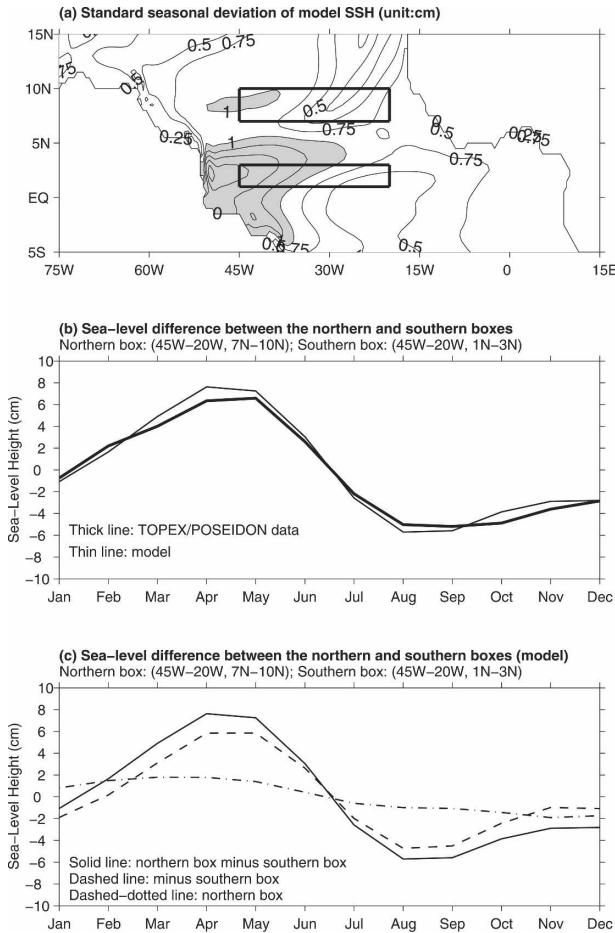
FIG. 8. (a) The standard seasonal deviation of model SSH deviation (cm). This is to compare with the T/P data shown in Fig. 2. (b) The difference of the SSH between two boxes, one to the north of NECC (7°–10°N, 45°–20°W) and the other to the south (1°–3°N, 45°–20°W). The thick line is from T/P data and the thin line is from the model result. These two lines compare very well for both amplitude and phase evolution. (c) The dashed line is for the SSH variation in the southern box (multiplied by −1) and the dash–dotted line is for the northern box. The SSH difference between these two boxes (solid line) is clearly dominated by changes in the southern box (dashed line).

strongest in August–October. In general, the model $\Delta\eta$ evolution (Fig. 9b) is quite similar to the data (Fig. 9a) except that the center of maximum variation in the model extends all the way from 40°W to the western boundary. We speculated earlier that this may be due to the model weakness in treating the broad shelf region off the western boundary as a deep basin (the reduced-gravity model assumes that the abyssal layer is very deep). Both the amplitude and the phase compare well with the data. The model SSH variation along each of the bounding latitudes is shown separately in Figs. 9c,d. It is interesting to note that the seasonal cycle of η along 3° and 10°N is almost exactly in opposite phase

(Figs. 9c,d) in both model and data (not shown here). So the contributions to the geostrophic velocity from $-\eta_{10N}$ and η_{3N} are exactly in the same phase. This is a very important fact that will help us to explain later why previous studies (e.g., Katz 1987) that used only the local forcing could reproduce well the observed seasonal cycle of NECC. We will defer the detailed discussion about this to section 4 after results from sensitivity tests are shown.

Now we briefly summarize the result from the standard model run and its comparison with the T/P altimetry data. Despite the model simplicity, it is doing reasonably well in simulating the basinwide seasonal SSH variability. The variation of geostrophic transport is mainly due to the SSH change in the southern flank of the NECC. The Ekman component of the NECC has a seasonal cycle that is in the same phase, though much weaker in amplitude, than geostrophic velocity.

b. Zero wind stress curl

We have designed a few experiments to test the hypothesis that the NECC transport is strongly influenced by the equatorial ocean dynamics. In this section we will show the result from a model experiment in which the wind stress has a zero curl. This sensitivity experiment is similar in principle (although a much simpler model is used here) to an OGCM experiment made by Philander and Pacanowski (1986) who examined the equatorial ocean's response to a wind stress that has a zero curl. Followed Philander and Pacanowski (1986), we set the meridional stress τ^y to be zero and the zonal stress to be the same as that at the equator:

$$\tau^x(\phi, \theta, t) = \tau^x(\phi, 0, t) \quad \text{and} \quad \tau^y(\phi, \theta, t) = 0. \quad (7)$$

The curl of the wind stress, curl $\boldsymbol{\tau} = -\partial\tau^x/\partial y$, is identical to zero. The same ocean model as in the standard run is then forced by wind stress described in (7) to a steady seasonal cycle (after running the model for 10 yr). It should be noted that the Ekman pumping related to the wind stress forcing in the extratropical ocean has the following form:

$$W_e = \text{curl}\, \frac{\boldsymbol{\tau}}{f\rho} = \frac{1}{f\rho} \text{curl}\, \boldsymbol{\tau} + \frac{\beta\tau_x}{f^2\rho}. \quad (8)$$

So even though the curl of the wind stress is zero, the local forcing mechanism is not necessarily absent due to the presence of the last term in (8). Because of $f = 0$ at the equator, it is practically difficult to design an experiment that would use the equatorial value of W_e over the whole basin. However, we will show later in section 4 that the forcing term associated with last term in (8) would contribute negatively to the observed NECC transport. In the other words, including the last
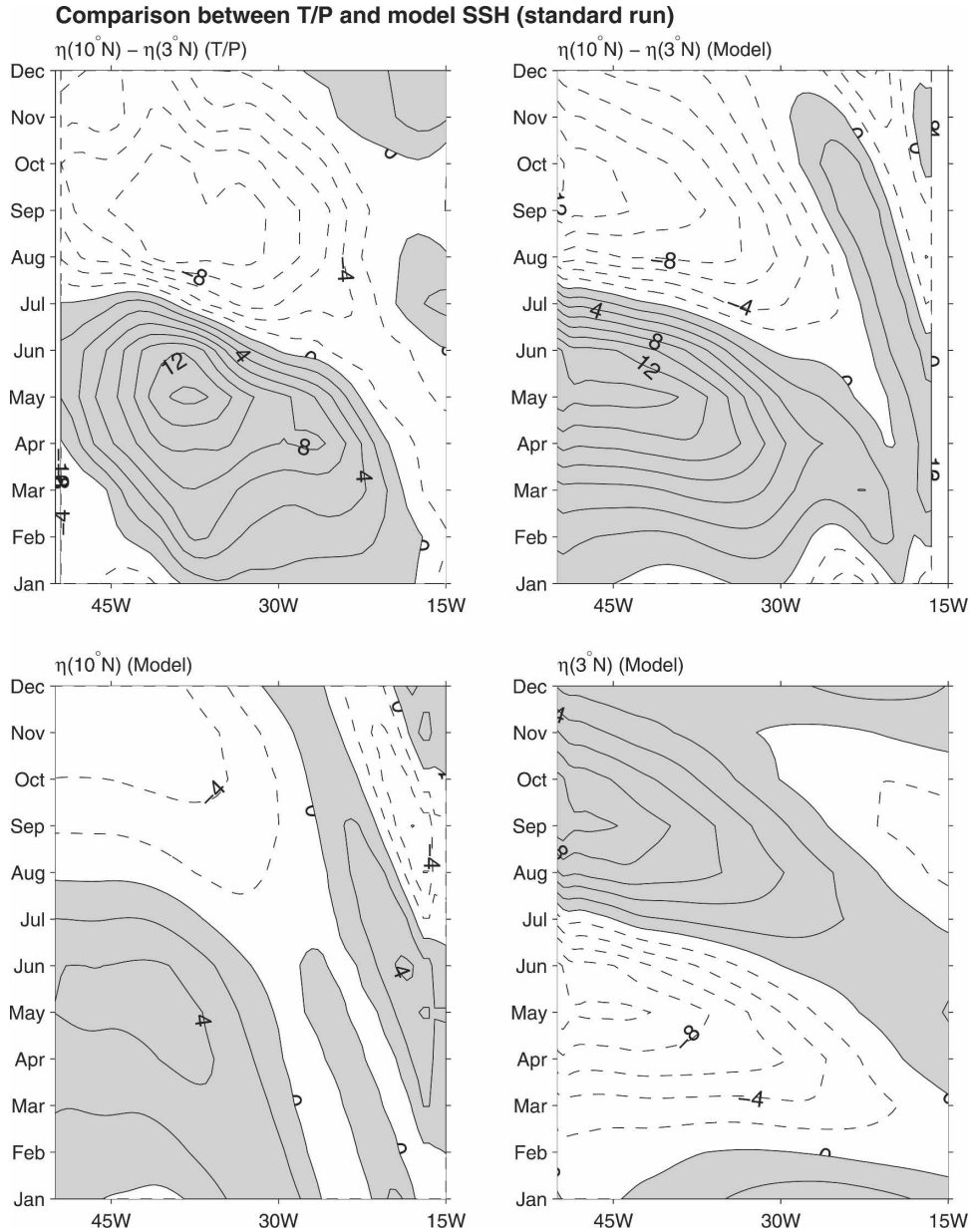
Comparison between T/P and model SSH (standard run)

FIG. 9. The time evolution of SSH η across the basin: (a) the difference of η between 10° and 3°N from T/P data, (b) the difference of η between 10° and 3°N from the model (standard run), (c) along 10°N, and (d) along 3°N.

term in (8) does not increase the contribution from the local forcing to the seasonal variability of the NECC transport.

Applying the forcing specified in (7), the model produces a seasonal SSH field, shown in Fig. 10, which is very similar to that from the standard run (Fig. 7) in lower-latitude regions. The difference from the standard run becomes more obvious toward higher latitudes, especially to the north of ITCZ, where the wind stress curl becomes the dominant forcing mechanism.

This time evolution $\Delta\eta$ between 10° and 3°N from this sensitivity test (Fig. 11a) has a very similar structure as that from the standard run (Fig. 9b) except that the amplitude is about 1/3 weaker. The weaker amplitude is mostly due to much smaller seasonal variability along 10°N. The η variability along 3°N is quite comparable to the standard run. The pattern of the averaged velocity field in the whole upper layer shows a high degree of similarity to the standard run. The weaker seasonal deviation in the velocity field is attributed to the lack of

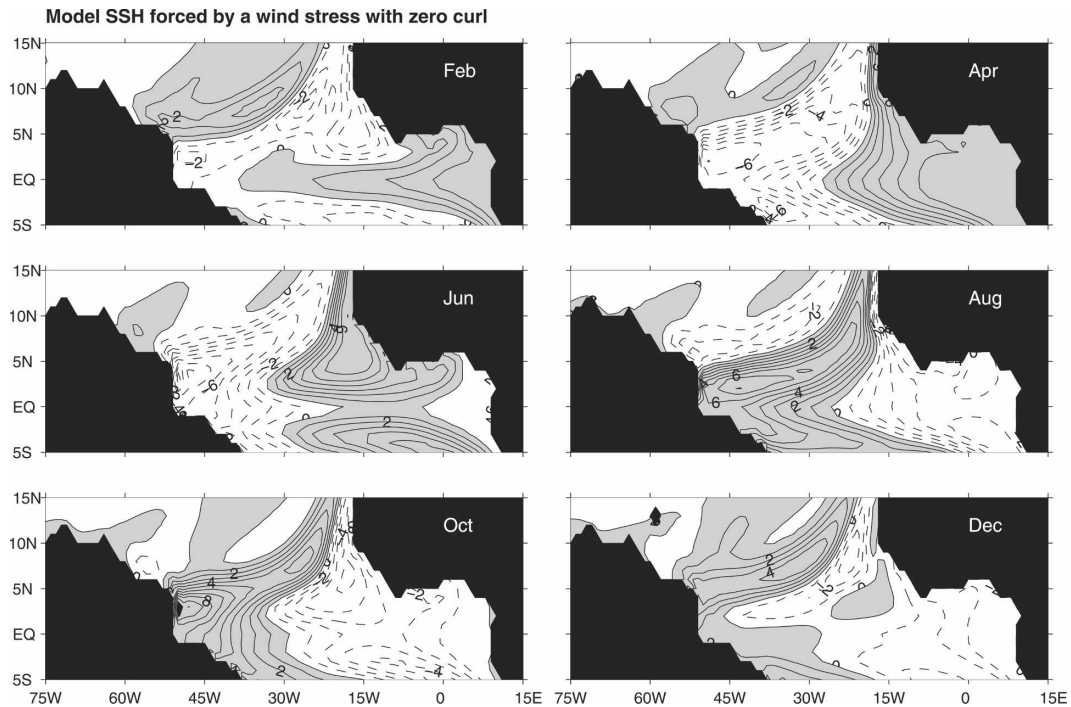**Model SSH forced by a wind stress with zero curl**

FIG. 10. Same as in Fig. 7 except that the wind stress has a zero curl.

wind stress curl forcing out of the equatorial zone. This sensitivity experiment shows that the seasonal variability of NECC is not merely due to the local forcing of wind stress curl. What is the forcing mechanism that can accounts for the 2/3 of seasonal variability of the NECC geostrophic transport? In the next experiment, we are going to examine the role of equatorial forcing.

c. Equatorial forcing

In this section we will show the result from a model experiment in which the seasonal wind stress is applied only within a narrow latitudinal band along the equator. Specifically, the model is forced by seasonally varying wind stress from 1.5°S to 1.5°N only. Poleward of
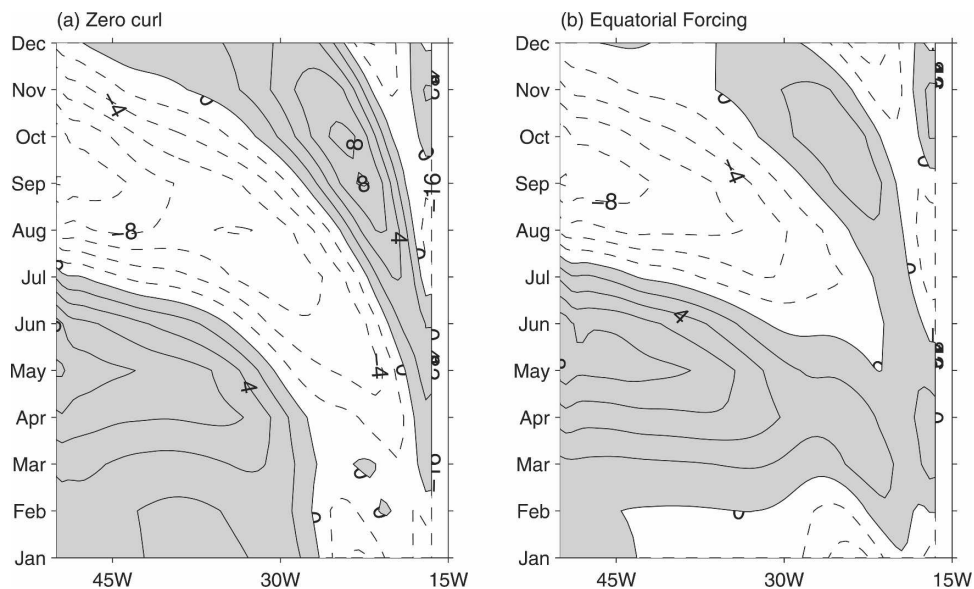

FIG. 11. The time evolution of SSH $\eta_{10N} - \eta_{3N}$ across the basin: from the experiment (a) with a zero curl and (b) with an equatorial forcing.

this band, only the steady annual-mean wind stress is used in the model:

$$\boldsymbol{\tau}(\phi, \theta, t) = \boldsymbol{\tau}_m(\phi, \theta) + \boldsymbol{\tau}'(\phi, \theta, t) \quad \text{for} \quad 1.5°\text{S} \le \theta \le 1.5°\text{N}$$

$$= \boldsymbol{\tau}_m(\phi, \theta) \quad \text{for} \quad \theta < 1.5°\text{S} \quad \text{or} \quad \theta > 1.5°\text{N},$$

$$(9)$$

where $\boldsymbol{\tau}_m$ and $\boldsymbol{\tau}'$ are the annual mean and seasonal deviation of surface wind stress. We should point out that cutting off the seasonal variation in the wind stress outside this equatorial band will probably result in abrupt changes of the wind stress curl along 1.5°S and 1.5°N. This could affect the dynamics near these two lines but should have less effect on the NECC, which is located farther north.

The seasonal deviation of the SSH η shows a broad similarity between this equatorial-forcing experiment with the standard run even in areas where no seasonal forcing is applied (not shown here). The upper-layer velocity (not shown here) captures the main seasonal variability of the NECC even though the local forcing is steady. The time evolution of SSH difference between 3° and 10°N is shown in Fig. 11b. When compared with the standard run, the SSH change along 10°N is much weaker in this experiment because of the steady extratropical forcing while the variability along 3°N is comparable between these two experiments (not shown here). The geostrophic transport in the sensitivity test is about 2/3 of the strength in the full forcing case (cf. Figs. 11b and 9b). This experiment demonstrates that the wind stress forcing in the equatorial ocean can influence the seasonal variability of the NECC.

The seasonal variability in regions poleward of 1.5° in either hemisphere has to be induced by equatorial dynamics. As reviewed by Philander (1990), the equatorial ocean's response to transient wind stress forcing involves equatorial Kelvin and Rossby waves and their reflections at the western and eastern boundaries. Through these propagation and reflection processes, waves that were originally formed in the equatorial ocean can remotely force extratropical ocean. Both equatorial Rossby waves and coastal Kelvin waves along the eastern boundary will be formed when an equatorial Kelvin wave reflects at the eastern boundary. Westward Rossby waves will be radiated offshore as coastal Kelvin waves propagate poleward to the higher-latitude ocean. Through this teleconnection, equatorial wind stress can remotely force interior regions outside the equatorial waveguide. This remote forcing mechanism in other oceans has been investigated [e.g., Yu et al. (1991) for the Indian Ocean]. For the purpose of verifying the role of this remote forcing mechanism in this sensitivity test, we have conducted

another experiment with the same forcing applied only to the equatorial band but with a very strong damping (sponge layer) applied within a longitudinal band of 2.5° along the eastern boundary. This was designed to dampen the remote forcing in associated with Rossby wave radiation from the eastern boundary. The model result (not shown here) reveals that the interior variability outside the equatorial band and especially in the central and eastern basin becomes much weaker, consistent with what is expected in a scenario without the remote forcing from the equator.

d. Experiment with hemispherically antisymmetrical forcing

In the previous two sensitivity experiments, we have demonstrated that 1) removing the curl of wind stress in the forcing field does not eliminate the seasonal cycle of the NECC, and 2) that applying zonal wind stress forcing only within a narrow equatorial band outside of NECC still produces a seasonal NECC variability that retains about 2/3 of the total transport variation. These two experiments seem to suggest that the equatorial forcing is a major forcing mechanism for the NECC seasonal cycle while wind stress curl is an important secondary contributor. The response of the equatorial ocean to transient wind stress forcing can be distinctly different depending on the meridional structure of the wind stress. For the seasonal time scale, the oceanic response consists of a set of hemispherically symmetrical waves, including equatorial Kelvin waves and odd-numbered-meridional-mode Rossby waves, and a set of antisymmetrical Rossby waves (the even-numbered modes). In most situations only Kelvin waves and the gravest modes of symmetrical (mode 1) and antisymmetrical (mode 2) waves are relevant. As we will discuss later, the oceanic response in the standard run is mainly from symmetrical waves. In the next experiment we will alter the wind stress in the Southern Hemisphere so that the oceanic response will be antisymmetrical waves. The wind stress in the Northern Hemisphere is the same as that used in the standard run. Specifically, the wind stress field is specified as the following:

$$\tau^x(\phi, -\theta, t) = -\tau^x(\phi, \theta, t) \quad \text{and}$$

$$\tau^y(\phi, -\theta, t) = \tau^y(\phi, \theta, t) \quad \text{for} \quad \theta < 0. \quad (10)$$

In a box model with symmetrical geometry, this antisymmetrical forcing will only excite even-numbered modes (antisymmetric modes) of Rossby, inertial-gravity, and Yanai waves. Because of the realistic geometry used in this model, however, we cannot completely eliminate the symmetrical modes but can greatly

The seasonal deviation of the zonal velocity at 35°W
(solid line: standard run; dashed line: modified wind stress in the southern hemisphere)

The seasonal deviation of the zonal velocity at 45°W
(solid line: standard run; dashed line: modified wind stress in the southern hemisphere)
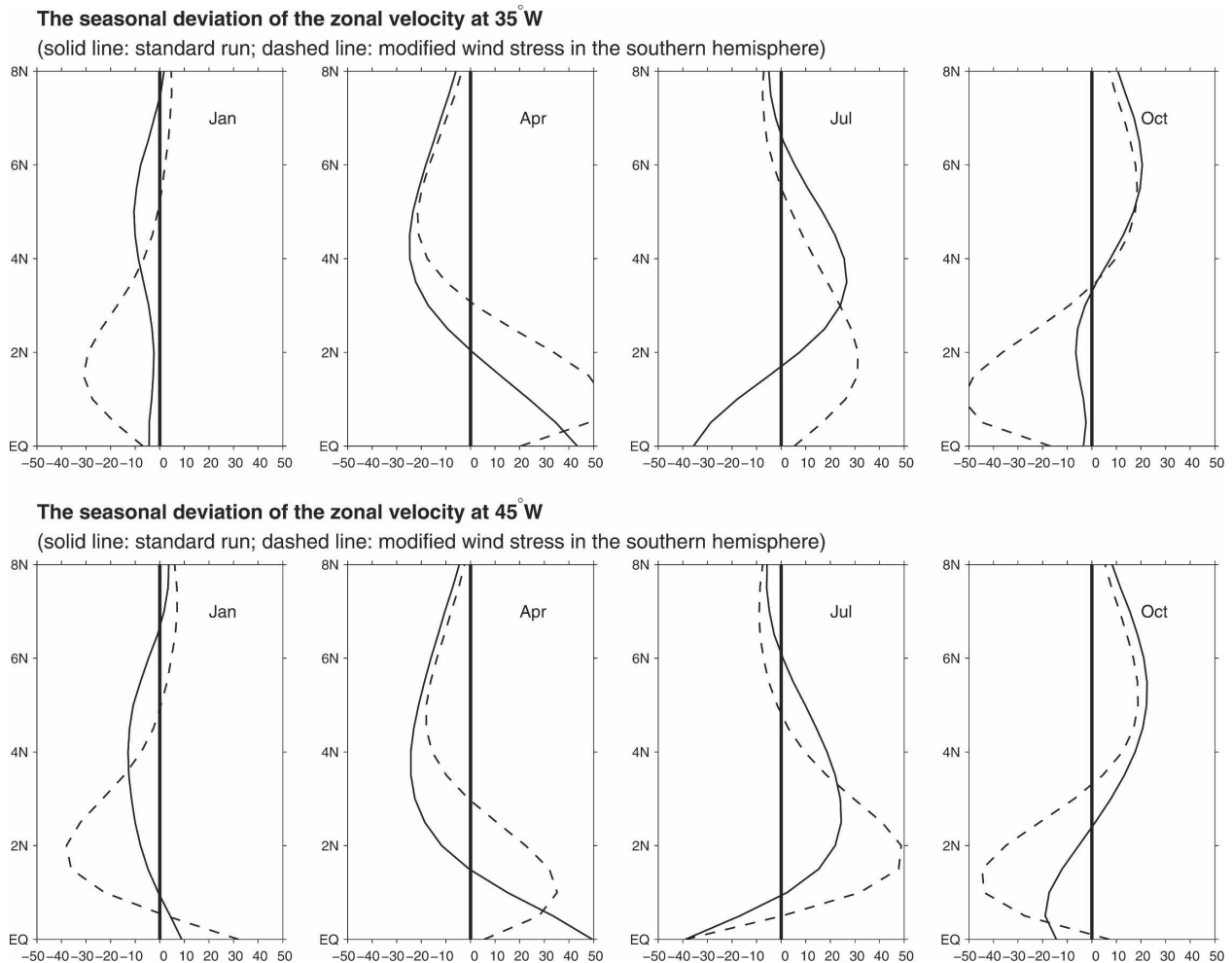

FIG. 12. The meridional profiles of zonal velocity at (top) 35° and (bottom) 45°W. Note the differences between the standard run (solid lines) and the antisymmetrical run (dashed lines) in which wind stress in the southern Atlantic Ocean is altered.

dampen them by using (10). An advantage of using (10) is that the wind stress and thus its curl in the Northern Hemisphere where the NECC is located are unchanged. Any deviation of the NECC from the standard run must come from the equatorial dynamics.

The seasonal deviation of the SSH from this "antisymmetrical experiment" is noticeably different from the standard run (not shown here) even in the Northern Hemisphere where the wind stress is unchanged. The difference between the two experiments appears to be greater in the summer than in winter months and in the eastern and central basin than in the western basin. The time evolution of η along 3° and 10°N and their difference indicates that the change is more evident in the lower-latitude region. The geostrophic transport between 3° and 10°N is not only weaker but its seasonal cycle is also shifted by about 1 month when compared with the standard run. The meridional profiles of the

zonal velocity for both the standard run and this antisymmetrical run in January, April, July, and October are shown in Fig. 12 (solid lines for the standard run and dashed lines for the antisymmetrical run). The velocity profiles taken at both 35° and 45°W clearly indicate that changing the wind stress in the Southern Hemisphere will have major effects on the northern tropical ocean. This remote effect is through the selection of meridional modes.

Next we will examine whether the seasonal variability is dominated by the symmetrical Rossby waves in the standard run and by antisymmetrical Rossby waves in this current run. Normalized meridional profiles of the zonal velocity component in March and August are shown by dashed lines in Fig. 13 [upper panels for the standard run and lower panels for the run using (10)]. We also plot here the velocity profiles that will be expected from the analytical solution for the mode-1 lin-

Normalized zonal velocity at 40°W for the symmetric forcing experiment
(dashed: model; solid: expected from linear wave theory)

Normalized zonal velocity at 40°W for the anti–symmetric forcing experiment
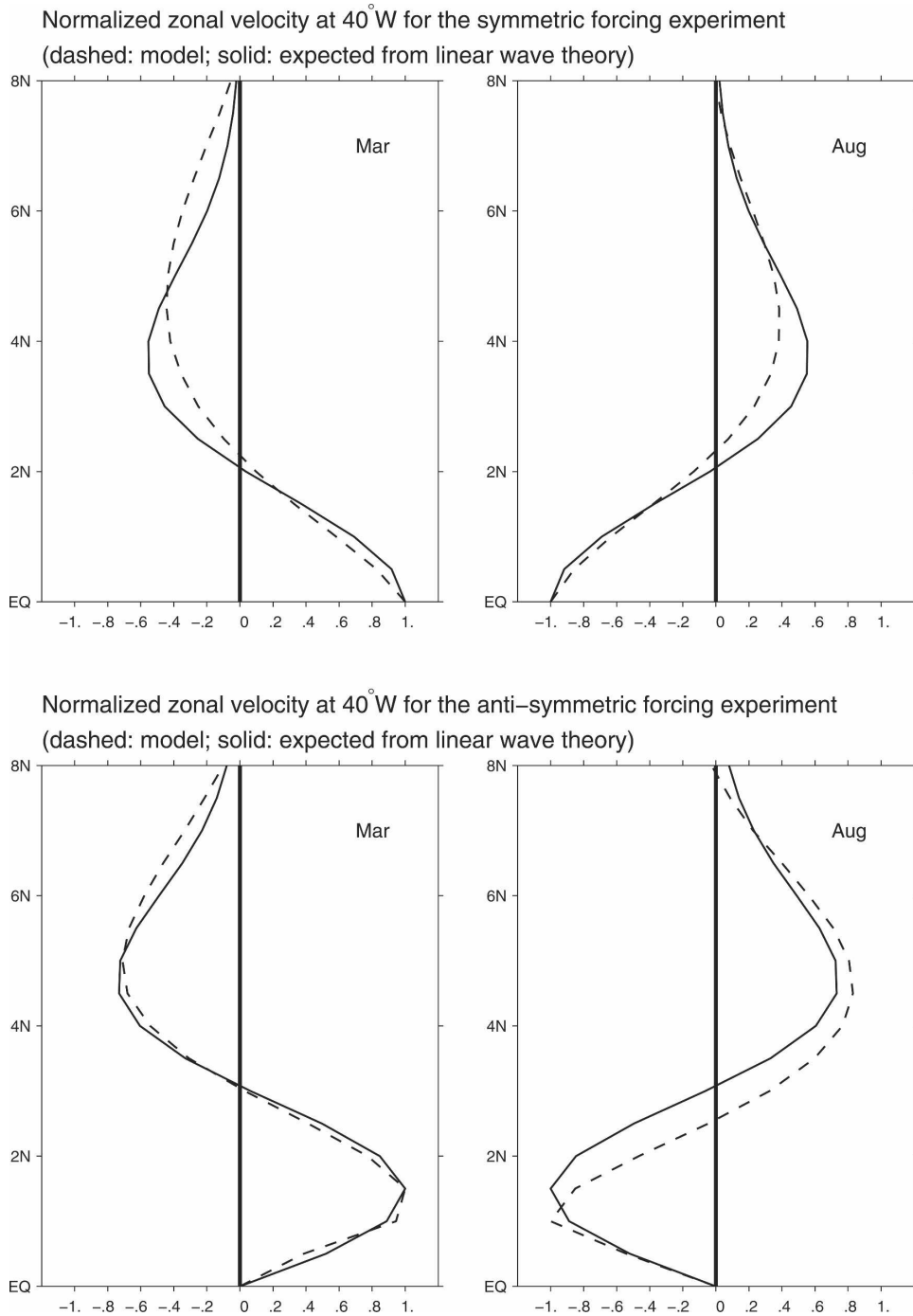(dashed: model; solid: expected from linear wave theory)

FIG. 13. (top) The comparison of the normalized zonal velocity profile from the standard run (dashed lines) and the meridional structure from the linear free mode-1 Rossby wave solution (solid lines). (bottom) The normalized velocity profile from the antisymmetrical run (dashed lines) and the linear free mode-2 Rossby wave.

ear and free Rossby waves (solid lines in the upper panels) and for the mode-2 linear and free Rossby waves (solid lines in the lower panels). The model appears to match the theoretical solution well. We must point out that the standard run must contain a signal from the equatorial Kelvin waves and that may explain some of the mismatch here. It is, however, quite amazing how well the model result from the antisymmetrical
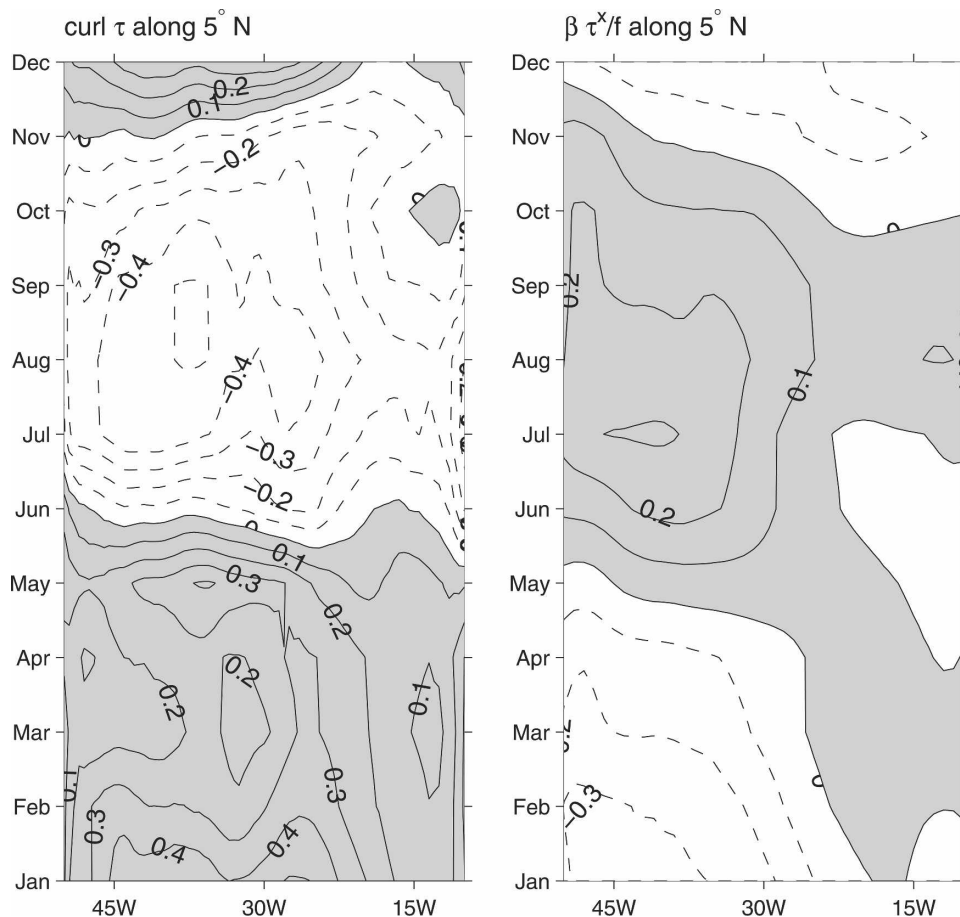
FIG. 14. The evolution of two forcing terms in (10). Note that they are nearly in opposite phase and the second term is weaker than the first term, so that the second term actually weakens the model's response to local wind stress forcing. The annual means in both plots have been removed. Unit is 10^{-8} N m^{-3}; contour interval is 10^{-9} N m^{-3}; areas with positive values are shaded.

run agrees with the mode-2 Rossby wave structure, especially in March.

Showing this experiment we try to demonstrate that changing wind stress in the Southern Hemisphere can affect the selection of equatorial modes and thus influence the ocean circulations in the northern tropical Atlantic Ocean. If the NECC were primarily forced by local wind stress curl, one would expect that the NECC would be the same as in the standard run since the forcing in the Northern Hemisphere is unchanged in this sensitivity run. The result here clearly further supports our hypothesis that the equatorial forcing is a main mechanism for the seasonal variability of the NECC.

4. Discussion and summary

In this study, we have examined the forcing mechanisms for the seasonal variability of the North Equatorial Countercurrent in the Atlantic Ocean. A simple

one-layer reduced-gravity model is used and its results are compared with satellite altimetry data. In the standard run, the model results compare well with the observed SSH seasonal cycle. We have shown results from three additional sensitivity runs to demonstrate that the wind stress forcing along the equator is the leading mechanism for the seasonal variability of the NECC geostrophic transport. The local wind stress curl makes an important secondary contribution (roughly about 1/3 of the geostrophic transport between 2° and 10°N is due to this forcing). It is puzzling, however, why Katz (1987) was able to reproduce well the seasonal cycle of NECC transport by using the local wind stress forcing only. Here we will try to reconcile the difference. The model used by Katz (1987) is a linear vorticity equation that excludes the equatorial processes:

$$\frac{\partial \eta}{\partial t} - c_R \frac{\partial \eta}{\partial x} = \frac{\Delta \rho}{\rho^2 f}\left(\operatorname{curl} \boldsymbol{\tau} + \frac{\beta \tau^x}{f}\right), \qquad (11)$$

where c_R is the phase speed of long Rossby waves and η is the dynamical height variation. For the geostrophic transport of NECC [i.e., $Hg'(\eta_{south} - \eta_{north})$], both model and altimetry data show that contributions from SSH variations in the south (η_{south}) and the north ($-\eta_{north}$) are in the same phase. So even without the equatorial forcing, the local forcing alone will produce a weaker (than observed) geostrophic transport that has the right phase due to SSH variation in the northern flank ($-\eta_{north}$). So the real issue is how to explain that the right amplitude that Katz (1987) was able to simulate. In Katz's model, he explicitly pointed out that he had to use $\Delta\rho/\rho = 4 \times 10^{-3}$ although his data indicated $\Delta\rho/\rho = 2$–2.5×10^{-3}. By using the larger density difference, the response of the dynamical height in (11) will be artificially amplified.

From (11) one notes that the curl of wind stress (i.e., the first term on the rhs) is not the only local forcing mechanism. There should be an additional term [i.e., the second term on the rhs of (11)]. This term was not excluded in the sensitivity test shown in section 3b. To show how important this term is, we plot the time evolution of both the first and the second terms in (11) along 5°N. Figure 14 shows the evolutions of both terms with the annual mean removed. It is interesting to note that they are nearly in opposite phase with the second term being weaker. In other words, the second term in (11) weakens the oceanic response to local wind stress curl forcing.

REFERENCES

Arnault, S., 1987: Tropical Atlantic geostrophic currents and ship drifts. *J. Geophys. Res.,* **92,** 5076–5088.

Atlas, R., R. N. Hoffman, and S. C. Bloom, 1993: Surface wind velocities over the ocean. *Atlas of Satellite Observations Related to Global Change,* R. J. Gurney, J. L. Foster, and C. L. Parkinson, Eds., Cambridge University Press, 128–139.

Busalacchi, A., and J. Picaut, 1983: Seasonal variability from a model of the tropical Atlantic Ocean. *J. Phys. Oceanogr.,* **13,** 1564–1588.

Cane, M. M. A., and E. S. Sarachik, 1983: Equatorial oceanography. *Rev. Geophys. Space Phys.,* **21,** 1137–1148.

Carton, J. A., and E. J. Katz, 1990: Estimates of the zonal slope and seasonal transport of the Atlantic North Equatorial Countercurrent. *J. Geophys. Res.,* **95,** 3091–3100.

Fratantoni, D. M., W. E. Johns, T. L. Townsend, and H. E. Hurlburt, 2000: Low-latitude circulation and mass transport pathways in a model of the tropical Atlantic Ocean. *J. Phys. Oceanogr.,* **30,** 1944–1966.

Garzoli, S., and E. Katz, 1983: The forced annual reversal of the Atlantic North Equatorial Countercurrent. *J. Phys. Oceanogr.,* **13,** 2082–2090.

——, and P. L. Richardson, 1989: Low-frequency meandering of the Atlantic North Equatorial Countercurrent. *J. Geophys. Res.,* **94,** 2079–2090.

Jochum, M., and P. Malanotte-Rizzoli, 2003: On the generation of North Brazil Current rings. *J. Mar. Res.,* **61,** 147–173.

Joyce, T. M., C. Frankignoul, J. Yang, and H. E. Phillips, 2004: Ocean response and feedback to the SST dipole in the tropical Atlantic. *J. Phys. Oceanogr.,* **34,** 2525–2540.

Katz, E. J., 1987: Seasonal response of the sea surface to wind in the equatorial Atlantic. *J. Geophys. Res.,* **92,** 1885–1893.

——, and S. Garzoli, 1982: Response of the western equatorial Atlantic Ocean to an annual wind cycle. *J. Mar. Res.,* **40,** 307–327.

——, and ——, 1984: Thermocline displacement across the Atlantic North Equatorial Countercurrent. *Geophys. Res. Lett.,* **11,** 737–740.

Koblinsky, C. J., B. D. Beckley, R. D. Ray, Y.-M. Wang, and A. Brenner, 1998: NASA Ocean Altimeter Pathfinder Project report 1: Data processing handbook. Goddard Tech. Memo., 55 pp.

Lee, S.-K., and G. T. Csanady, 1999: Warm water formation and escape in the upper tropical Atlantic Ocean: 1. A literature review. *J. Geophys. Res.,* **104,** 29 561–29 571.

Liu, W. T., W. Tang, and R. Atlas, 1996: Responses of the tropical Pacific to wind forcing as observed by spaceborne sensors and simulated by an ocean general circulation model. *J. Geophys. Res.,* **101,** 16 345–16 359.

McCreary, J. P., J. Picaut, and D. W. Moore, 1984: Effect of annual remote forcing in the eastern tropical Atlantic. *J. Mar. Res.,* **42,** 45–81.

Moore, D. W., and S. G. H. Philander, 1977: Modelling of the tropical ocean circulation. *The Sea,* E. D. Goldberg et al., Eds., Marine Modeling, Vol. 6, John Wiley and Sons, 319–361.

Philander, S. G. H., 1990: *El Nino, La Nina, and the Southern Oscillation.* Academic Press, 293 pp.

——, and R. C. Pacanowski, 1986: A model of the seasonal cycle in the tropical Atlantic Ocean. *J. Geophys. Res.,* **91,** 14 192–14 206.

Richardson, P. L., and T. K. McKee, 1984: Average seasonal variation of the Atlantic Equatorial Currents from historic ship drifts. *J. Phys. Oceanogr.,* **14,** 1226–1238.

——, and D. Walsh, 1986: Mapping climatological seasonal variations of surface currents in the tropical Atlantic using ship drifts. *J. Geophys. Res.,* **91,** 10 537–10 550.

——, and S. G. H. Philander, 1987: The seasonal variations of surface currents in the tropical Atlantic Ocean: A comparison of ship drift data with results from a general circulation model. *J. Geophys. Res.,* **92,** 715–724.

——, and G. Reverdin, 1987: Seasonal cycle of velocity in the Atlantic North Equatorial Countercurrent as measured by

surface drifts, current meters, and ship drifts. *J. Geophys. Res.,* **92,** 3691–3708.

——, S. Arnault, S. Garzoli, and J. G. Bruce, 1992: Annual cycle of the Atlantic North Equatorial Countercurrent. *Deep-Sea Res.,* **39,** 997–1014.

Schouten, M. W., R. P. Mattano, and T. P. Trub, 2005: A description of the seasonal cycle of the equatorial Atlantic from altimeter data. *Deep-Sea Res.,* **52,** 477–493.

Verdy, A., and M. Jochum, 2005: A note on the validity of the Sverdrup balance in the Atlantic North Equatorial Countercurrent. *Deep-Sea Res.,* **52,** 179–188.

Waliser, D. E., and C. Gautier, 1993: A satellite-derived climatology of the ITCZ. *J. Climate,* **6,** 2162–2174.

Yu, L., J. J. O'Brien, and J. Yang, 1991: On the remote forcing of the circulation in the Bay of Bengal. *J. Geophys. Res.,* **96,** 20 449–20 454.

Zebiak, S. E., and M. A. Cane, 1987: A model of El Niño-Southern Oscillation. *Mon. Wea. Rev.,* **115,** 2262–2278.